Applied Surface Science 258 (2011) 898–907

Contents lists available at SciVerse ScienceDirect

Applied Surface Science

journal homepage: www.elsevier.com/locate/apsusc

Solute transport and composition profile during direct metal deposition with coaxial powder injection

Xiuli He[a,*], Lijun Song[b], Gang Yu[a], Jyoti Mazumder[b]

[a] Key Laboratory of Mechanics in Advanced Manufacturing, Institute of Mechanics, Chinese Academy of Sciences, Beijing 100190, People's Republic of China
[b] Center for Laser-Aided Intelligent Manufacturing, University of Michigan, Ann Arbor, MI 48109, USA

ARTICLE INFO

Article history:
Received 14 April 2011
Received in revised form 26 August 2011
Accepted 7 September 2011
Available online 16 September 2011

PACS:
81.16.Mk (laser-assisted deposition)
82.20.Wt (computational modelling; simulation)

Keywords:
Laser cladding
Solute transport
Composition profile

ABSTRACT

Direct metal deposition (DMD) with coaxial powder injection allows fabrication of three-dimensional geometry with rapidly solidified microstructure. During DMD, addition of powder leads to the interaction between laser and powder, and also the redistribution of solute. The concentration distribution of the alloying element is very important for mechanical properties of the deposited clad material. The evolution of concentration distribution of carbon and chromium in the molten pool is simulated using a self-consistent three-dimensional model, based on the solution of the equations of mass, momentum, energy conservation and solute transport in the molten pool. The experimental and calculated molten pool geometry is compared for model validation purposes.

shows the computed concentration profile of carbon as a function of location along the *x* direction, the intersection of symmetric plane and top surface. It can be seen that the concentration profile of carbon fluctuate at 0.4 wt%, the concentration of carbon in H13 powder. Fig. 4

1. Introduction

DMD involves complex physical phenomena, such as laser–powder interactions, heat transfer, melting, fluid flow and solidification. Many analytical and numerical models were developed for heat transfer and fluid flow. They were summarized by the authors in another publication [1].

During DMD with coaxial powder injection, addition of powder particles leads to the interaction between laser and powder, and also the redistribution of solute. Attenuation of laser power during interaction between a laser and powder was investigated a lot [2–15]. Qi et al. [2] considered the coaxial laser powder interaction while modelling heat transfer and fluid flow during DMD. A semi-empirical method of evaluating the laser energy redistribution during CO_2 laser cladding with lateral powder injection was reported by Gedda et al. [5]. It was found that 50% of the laser power was reflected off the cladding melt, 10% was reflected off the powder cloud, 30% was used to heat the substrate, and 10% was used to melt the clad layer. Lin [6,7] studied the laser attenuation and powder temperature distribution in a focused coaxial powder stream both experimentally and theoretically. A Gaussian distribution of coaxial powder concentration was used in his calculations and verified by experimental observation. Similar studies with a powder jet originating from a point source were conducted by Neto and Vilar [8]. Liu and Lin [9] studied, through a numerical model, the heating, melting and evaporation processes of a single spherical powder particle when irradiated by a CO_2 laser beam in coaxial powder flow cladding process. The laser energy, initial powder velocity and size have been shown to have important effects on the temperature profile of the powder stream. Kaplan and Groboth [10] developed an analytical model of laser cladding based on balances of mass and energy, which can calculate the temperature distribution in the workpiece. It was found that the powder catchment efficiency and the beam energy redistribution in the material can be optimized by the powder mass flow rate and geometrical properties of the beam and powder jet. An analytical model was presented by Fu et al. [11], in which a powder injection angle was introduced to enable the analysis for both coaxial and lateral powder flows. Formulations for divergent or attenuated laser beams were also given in their model for possible analytical solutions of attenuated energy distribution. Partes [12] developed an analytical model to evaluate the catchment efficiency for the laser cladding

* Corresponding author.
E-mail address: xlhe@imech.ac.cn (X. He).

0169-4332/$ – see front matter © 2011 Elsevier B.V. All rights reserved.
doi:10.1016/j.apsusc.2011.09.023

process at high processing speeds. It was concluded that the influence of the particles melting during the flight on the catchment efficiency was growing with increasing speed, laser power and powder feed rate. Brückner et al. [13] investigated the influence of process parameters such as feed rate and heat input on the residual stresses of cladding bead by an analytical model, including the powder–beam interaction, the powder catchment by the molten pool, and the self-consistent calculation of temperature field and bead shape. Huang et al. [14,15] introduced the classical optical theory to calculate the interaction between laser beam and powder stream and investigated the effect of powder feeding rate on the laser intensity and temperature of the particles. They found that the laser intensity distribution and the temperature of the particles at different sites on the surface of the workpiece tended to be even.

Pinkerton and Li [16] constructed a model to describe the variation in powder stream concentration along the axis of a coaxial nozzle. It related directly to nozzle dimensions, material mass and volume flow rates, and was sufficiently simple not to rely on numerical techniques. Lin [17] simulated the powder flow structures of a coaxial nozzle for laser cladding with various arrangements of the nozzle exit. The results showed that more than 50% powder concentration can be increased in a gas stream through a specific nozzle arrangement for coaxial laser cladding. Liu and Li [18] investigated the effects of powder concentration distribution on fabrication of thin-wall parts in coaxial laser cladding. They found that increase in concentration distribution led to decrease in wall thickness and increase in wall growing rate.

In some laser manufacturing processes, such as laser dissimilar welding, laser alloying and laser cladding, there exists solute redistribution, besides mass, momentum and energy transfer. The composition profiles in the molten pool have been simulated by solving the coupled momentum, energy, and species conservation equations for laser dissimilar welding [19,20] and laser alloying [21–25]. However, for laser cladding, few researchers have tried to simulate the solute transport process. Kar and Mazumder [26] determined the one-dimensional composition of extended solid solution based on the transport of energy and mass in laser cladding process. They solved governing equations analytically and predicted the extended solubility in clad with the continuous growth model. Huang et al. [27] simulated the mass transfer in the molten pool in the process of laser cladding. The concentration distribution on different sides of the interface between cladding layer and substrate was calculated separately and coupled at the co-boundary.

In previous work, He and Mazumder mainly investigated the heat transfer, fluid flow and energy distribution during single-track laser cladding [1], and the temperature and composition profile of the overlap region for double-track laser cladding [28]. In this study, the solute transport and composition profile evolution by single track during coaxial laser cladding is simulated by a self-consistent three dimensional numerical model, in which some important physical phenomena including melting and solidification, phase changes, mass addition, and interactions between the laser beam and the coaxial powder flow are considered.

2. Mathematical modelling

A numerical model to simulate heat transfer, fluid flow and mass transfer during laser cladding has been developed. Following assumptions are made in order to simplify calculations:

(1) The fluid motion in the molten pool is assumed to be Newtonian, laminar and incompressible.
(2) The thermo-physical properties of powder are considered the same as those of substrate, and these properties are assumed to be temperature-independent.

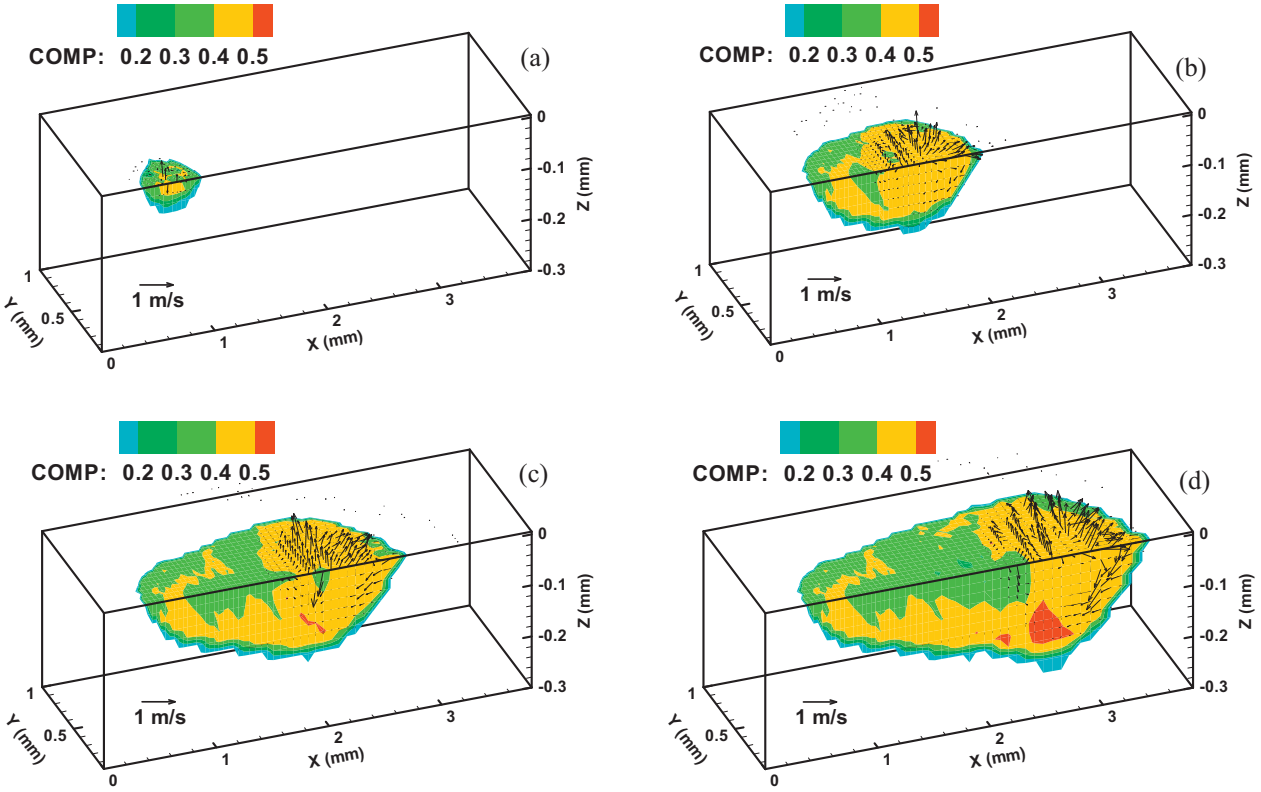

Fig. 1. Computed concentration profile of carbon at top surface and symmetric plane at different times: (a) $t = 200$ ms, (b) $t = 400$ ms, (c) $t = 600$ ms, and (d) $t = 800$ ms.

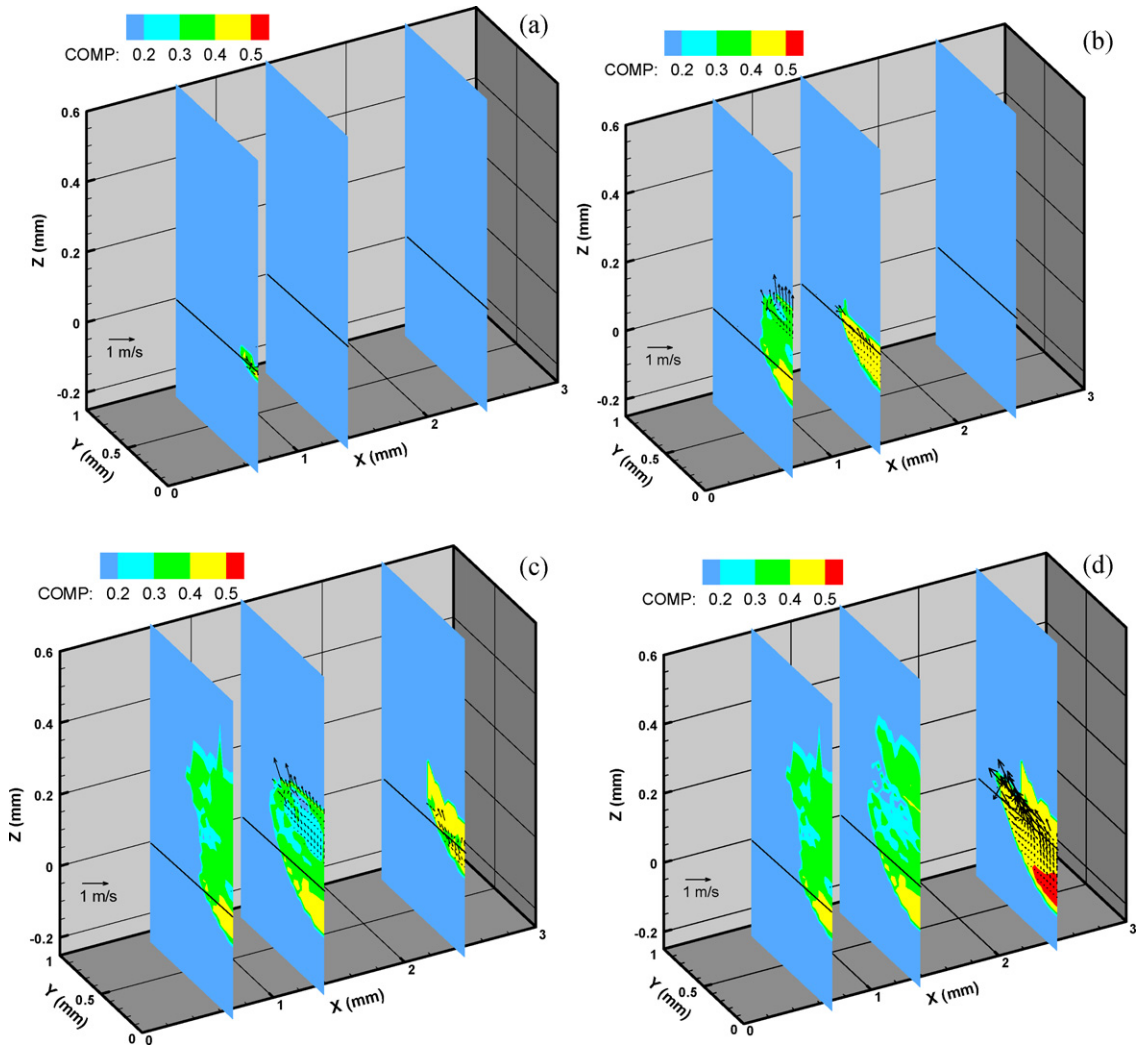

Fig. 2. Computed concentration profile of carbon along three planes of $x = 0.7$ mm, 1.4 mm, and 2.5 mm at different times: (a) $t = 200$ ms, (b) $t = 400$ ms, (c) $t = 600$ ms, and (d) $t = 800$ ms.

(3) The input heat from laser is assumed to have Gaussian distribution. The beam radius and profile keep constant along z direction. The absorption coefficient remains constant.
(4) There is no diffusion transport in solid phase.
(5) The spatial concentration profile of a converged coaxial powder flow is assumed to be a Gaussian distribution. The shape of powder particles is spherical. Powders falling in the region of liquid surface get melted immediately.

The details of the laser–powder interaction and free surface tracking have been shown in authors' previous publication [1], which is not repeated here.

2.1. Continuum model

The computational domain contains all three phases – solid, liquid and gas. The interface between gas and non-gas phases can be considered physically sharp, and tracked by the level-set method [1]. The physical properties are taken in gas and non-gas phases, respectively. For liquid–solid interface, due to the absorption or release of latent heat, phase change problems are nonlinear. Moreover, the liquid–solid interface in a multi-constituent alloying system can be morphologically unstable and forms a mushy zone which contains a mixture of both phases. In the study, the solid and liquid phases are treated as a continuum media, where the mushy zone is a porous solid with isotropic permeability [29]. Assuming that f and g represent the mass and volume fraction, respectively, the physical properties for a mixture of solid and liquid phase are defined as follows [30,31]:

$$\rho = g_s\rho_s + g_l\rho_l \tag{1}$$

$$k = \left(\frac{g_s}{k_s} + \frac{g_l}{k_l}\right)^{-1} \tag{2}$$

$$C_P = f_s C_{Ps} + f_l C_{Pl} \tag{3}$$

$$c = f_s c_s + f_l c_l \tag{4}$$

$$D = f_l D_l \tag{5}$$

where ρ is the density, k is the thermal conductivity, C_P is the specific heat, c is the solute concentration, D is the mass diffusivity. The subscripts s and l denote the solid and liquid phase, respectively.

2.2. Governing equations

Using the defined mixture variables in the mushy zone, the mass, momentum, energy conservation and species transport can be expressed in a binary S/L phase system by following governing equations, respectively.

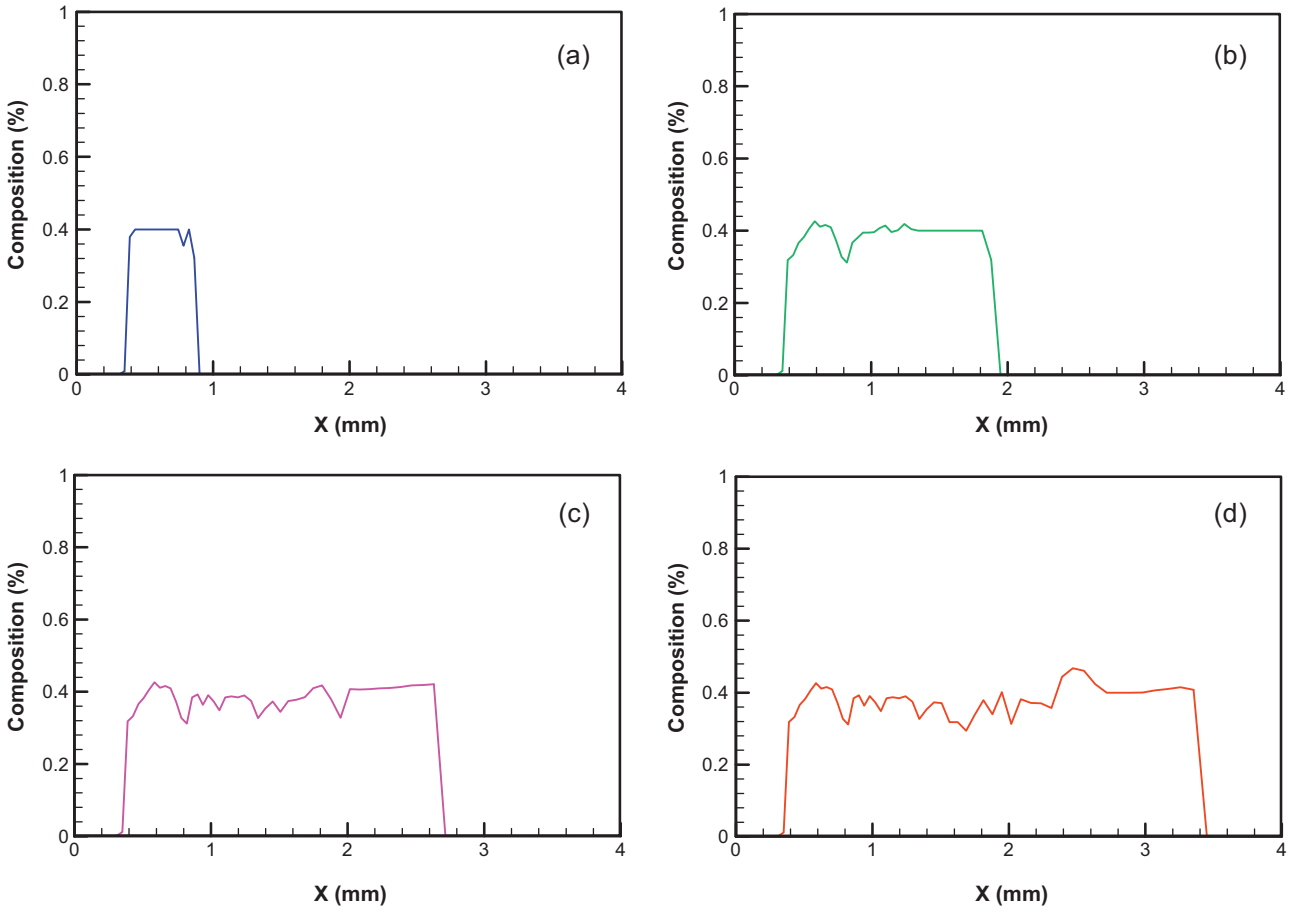

Fig. 3. Computed concentration profile of carbon as a function of location along the x direction at different times: (a) $t = 200$ ms, (b) $t = 400$ ms, (c) $t = 600$ ms, and (d) $t = 800$ ms.

Continuity equation:

$$\frac{\partial \rho}{\partial t} + \nabla \cdot (\rho \mathbf{u}) = 0 \tag{6}$$

Momentum equations:

$$\frac{\partial (\rho u)}{\partial t} + \nabla \cdot (\rho \mathbf{u} u) = \nabla \cdot (\mu \nabla u) - \frac{\mu_l}{K} \frac{\rho}{\rho_l} u - \frac{\partial p}{\partial x} \tag{7}$$

$$\frac{\partial (\rho v)}{\partial t} + \nabla \cdot (\rho \mathbf{u} v) = \nabla \cdot (\mu \nabla v) - \frac{\mu_l}{K} \frac{\rho}{\rho_l} v - \frac{\partial p}{\partial y} \tag{8}$$

$$\frac{\partial (\rho w)}{\partial t} + \nabla \cdot (\rho \mathbf{u} w) = \nabla \cdot (\mu \nabla w) - \frac{\mu_l}{K} \frac{\rho}{\rho_l} w - \frac{\partial p}{\partial z} + \rho g \beta (T - T_0) \tag{9}$$

Energy equation:

$$\frac{\partial (\rho C_P T)}{\partial t} + \mathbf{u} \cdot \nabla (\rho C_P T) = \nabla \cdot (k \nabla T) - \frac{\partial (\rho f_s \mathcal{L})}{\partial t} + \frac{\partial (\rho f_s \Delta \bar{C}_P T)}{\partial t} \tag{10}$$

Concentration equation:

$$\frac{\partial (\rho c)}{\partial t} + \nabla \cdot (\rho \mathbf{u} c) = \nabla \cdot (\rho D \nabla c) + \nabla \cdot [\rho D \nabla (c_l - c)] - \nabla \cdot [\rho f_s (c_l - c_s) \mathbf{u}] \tag{11}$$

where t is the time, u, v, and w are the liquid velocity along the x, y, and z direction, respectively, μ is the viscosity, p is the pressure, T is the temperature. The second term in the right side of Eqs. (7)–(9) is a Darcy term, representing the damping force when fluid is passing through a porous media, K is the isotropic permeability, which is assumed to vary with liquid volume fraction according to Kozeny–Carman equation [32]

$$K = K_0 \frac{g_l^3}{(1 - g_l)^2} \tag{12}$$

where K_0 is an empirical constant determined by the morphology of the porous media. The last term in Eq. (9) represents the buoyancy force, β is the thermal expansion coefficient. The last two terms in Eq. (11) account for the species flux due to the relative phase diffusion and motion, respectively. They are equivalent to zero when applied in pure liquid or solid phase.

2.3. Boundary conditions

A three-dimensional Cartesian coordinate system is used in the calculation, while only half of the workpiece is considered because of symmetry. The boundary condition at liquid/gas interface for energy equation can be formulated as

$$q_{L/G} = \frac{2Q'\eta}{\pi r_b^2} \exp\left(\frac{-2r^2}{r_b^2}\right) + q_P - h_c(T - T_0) - \sigma\varepsilon(T^4 - T_0^4) - \rho_l L_v F_e \tag{13}$$

The five terms in the right side represent the energy by the laser beam, the addition of the heated powder, and the heat loss by radiation, convection and evaporation, respectively. Q' is the attenuated laser power density, η is the laser absorption coefficient, r_b is the effective beam radius, r is the radial distance to the laser beam, h_c is the heat transfer coefficient, σ is the Stefan–Boltzmann constant, ε is the emissivity, T_0 is the ambient temperature, L_v is the

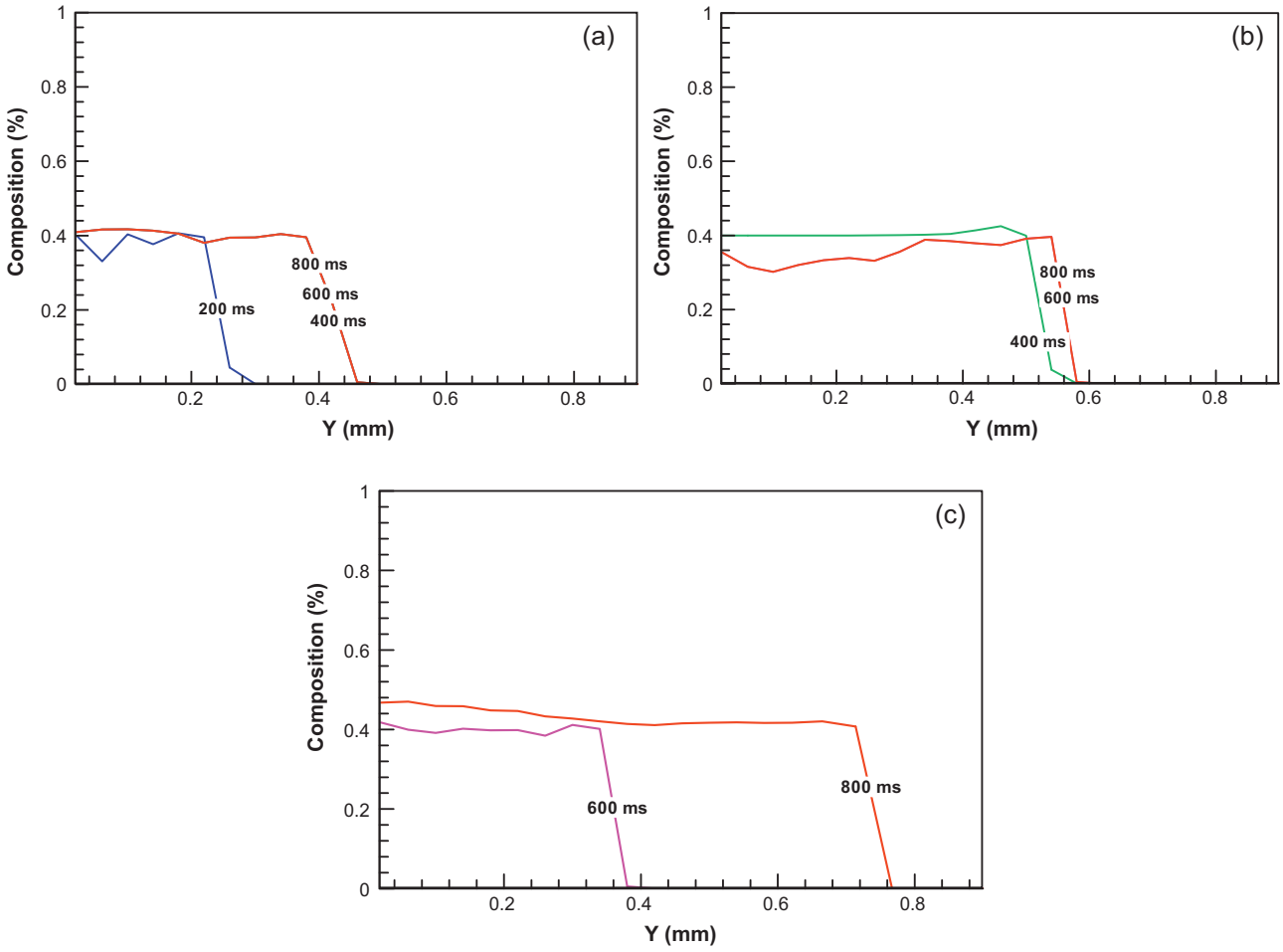

Fig. 4. Computed concentration profile of carbon as a function of location along the y direction for three different planes of (a) $x = 0.7$ mm, (b) $x = 1.4$ mm, and (c) $x = 2.5$ mm.

latent heat of evaporation, F_e is the evaporation flux. The absorption coefficient, η, is related to the electrical resistivity of the material and the wavelength of the infrared laser radiation by the following relation [33]:

$$\eta(T) = 0.365\left(\frac{\alpha}{\lambda}\right)^{1/2} - 0.0667\left(\frac{\alpha}{\lambda}\right) + 0.006\left(\frac{\alpha}{\lambda}\right)^{3/2} \quad (14)$$

where λ is the wavelength, and α is the electrical resistivity of the material. For CO_2 laser and low carbon steel, the laser absorption coefficient used in the calculation is 0.1.

Two forces are considered at liquid/gas interface – the capillary and thermocapillary forces. The capillary force acts in the normal direction due to the interface curvature and surface tension. The thermocapillary force acts in the tangential direction of the liquid free surface, and is caused by the surface temperature gradient. These forces can be formulated as

$$F_{L/G} = \sigma \mathbf{n}^* \kappa - \nabla_s T \frac{d\sigma}{dT} \quad (15)$$

where σ is the surface tension, $\mathbf{n}^*$ is the normal of surface pointing inward to liquid phase, κ is the curvature.

During an equilibrium solidification process, solute atoms are rejected from the solidification front and diffuse into the liquid phase. The boundary condition at the solidification interface can be given by the gradient of solute concentration on the liquid side

$$-D_l \frac{\partial c_l}{\partial n} = (1 - k_p) v_n c_l \quad (16)$$

where n is the direction of outward normal, v_n is the interface velocity in that direction. As the powder with a known composition of mixed material (c_p) is continuously deposited onto the molten pool surface, the boundary condition at the liquid/gas interface is

$$c|_{\varphi=0} = c_p \quad (17)$$

where φ is the level-set function [1]. For liquid–gas interface, $\varphi = 0$.

If the solidification speed is fast enough to suppress the diffusive speed of the solute atoms jumping across the S/L interface, the solute atoms may be trapped in the solid phase, which results in the formation of metastable extended solid solution. In the study, in order to account for the reduction of the diffusive flux at the solidification interface due to the fast solidification speed, a nonequilibrium partition coefficient model developed by Kar and Mazumder [34] is employed.

2.4. Solutions

Spatially nonuniform grids are adopted within the computational domain for maximum resolution of variables. A finer grid spacing is used near the heat source. In the calculation, a relaxation factor of 0.7 is chosen for the solving variables to avoid unpredicted divergence. With appropriate boundary conditions, the mass, momentum, energy conservation and species transport equations are discretized using control volume method and then solved using a Symmetrically Coupled Gauss Seidel (SCGS) point relaxation scheme [35]. Typically, the time step is restricted to be no more than 10^{-5} s to satisfy the convergence criteria requested

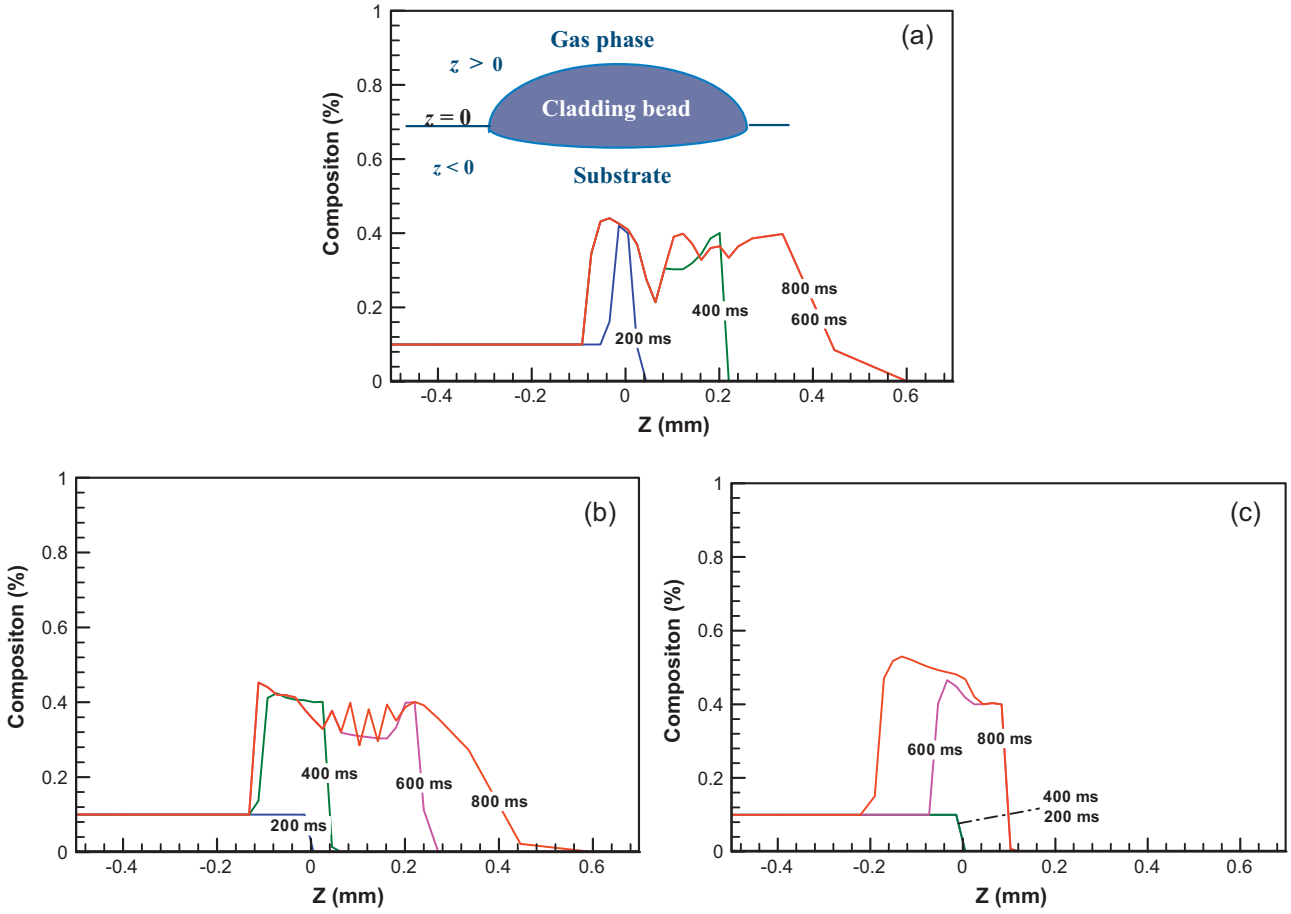

Fig. 5. Computed concentration profile of carbon as a function of location along the z direction for three different planes of (a) $x = 0.7$ mm, (b) $x = 1.4$ mm, and (c) $x = 2.5$ mm.

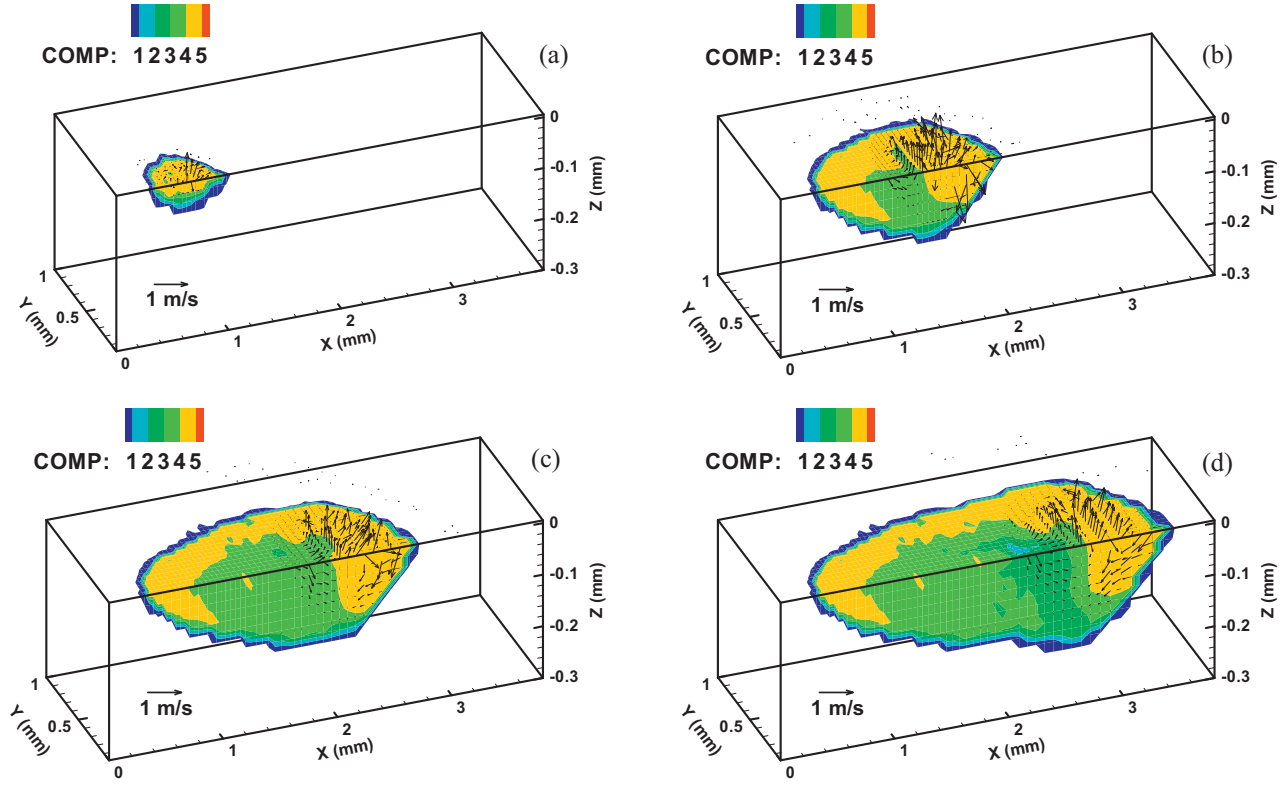

Fig. 6. Computed concentration profile of chromium at top surface and symmetric plane at different times: (a) $t = 200$ ms, (b) $t = 400$ ms, (c) $t = 600$ ms, and (d) $t = 800$ ms.

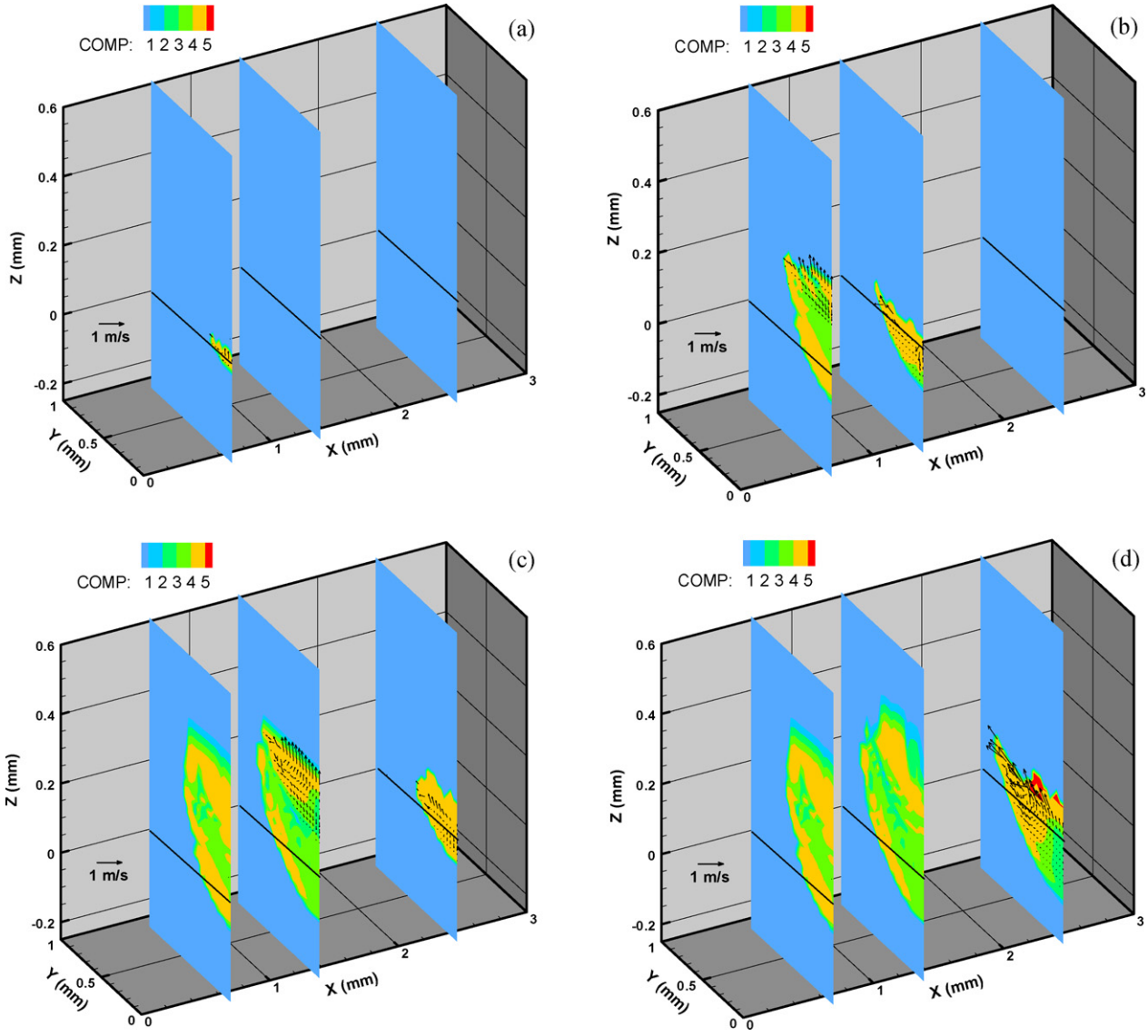

Fig. 7. Computed concentration profile of chromium along three planes of $x = 0.7$ mm, 1.4 mm, and 2.5 mm: (a) $t = 200$ ms, (b) $t = 400$ ms, (c) $t = 600$ ms, and (d) $t = 800$ ms.

by the governing equations, as well as the movement of the liquid/gas interface. The maximum displacement of the free surface at one time step should be less than the minimum grid spacing.

2.5. Parameters used in calculation and experiments

Laser cladding experiments were performed by depositing ANSI H13 tool steel powder on low carbon steel substrate by single track in a CO_2 laser. The composition measurement after laser cladding were conducted by Energy Dispersive X-Ray Spectroscopy (EDS), attached to Philips XL30 FEG Scanning Electron Microscope (SEM). The composition of alloying elements of H13 is shown in Table 1. The concentration of carbon and chromium is taken as 0.4 wt% and 5 wt% in H13 powder, and 0.1 wt% and 0.5 wt% in low carbon steel substrate, respectively. The data used for calculations [2,36] are presented in Table 2. The processing parameters used in the whole paper is as follows: laser power: 1900 W; beam

Table 1
The composition of alloying elements in H13 powder (wt%).

Element	Min	Max
Carbon	0.37	0.42
Manganese	0.2	0.5
Phosphorus	0	0.025
Sulfur	0	0.005
Silicon	0.2	0.8
Chromium	5	5.5
Vanadium	0.8	1.2
Molybdenum	1.2	1.75

Table 2
Data used for calculations.

Property	Value
Absorption coefficient	0.1
Liquid density (kg/m^3)	6518.5
Solid density (kg/m^3)	7870.0
Liquid viscosity (N-s/m^2)	0.005
Solidus temperature (K)	1776
Liquidus temperature (K)	1800.4
Latent heat of fusion (J/kg)	2.72×10^5
Solid specific heat (J/kg-K)	658.63
Liquid specific heat (J/kg-K)	804.03
Solid thermal conductivity (W/m-K)	40.96
Liquid thermal conductivity (W/m-K)	43.99
Surface tension coefficient (N/m-K)	−0.00049
Mass diffusivity (m^2/s)	3.0×10^{-8}
Thermal expansion coefficient (1/K)	1.45×10^{-4}

diameter: 1.8 mm; scanning speed: 200 mm/min; powder flow rate: 8 g/min.

3. Results and discussions

3.1. Concentration profile of carbon

During coaxial laser cladding processes, the addition of powder leads to the interaction of laser and powder, and also the redistribution of solute. Powder particles are heated by the laser beam and their temperature rises under irradiation by the laser, even accompanied by the phase transformation. They also accumulate energy, which is finally transmitted to the substrate. Meanwhile, the laser beam gets attenuated by absorption, reflection and scattering effects of the clouded particles. The temperature distribution of powder flow and the power intensity distribution of the attenuated laser beam are important boundary conditions on the liquid–gas interface.

The interaction between laser and powder, including the powder temperature and attenuation of laser power due to powder addition, has been investigated in previous work [1,2]. Only results of solute transport and composition profile are presented here. Fig. 1(a)–(d) shows the computed concentration profile of carbon during laser cladding with powder injection at different times. The concentration is indicated by wt%. The black arrows in the figures represent the velocity of the liquid metal. The origin represents the starting point of the laser beam. Fig. 2(a)–(d) shows the computed concentration profile of carbon on planes perpendicular to the laser scanning direction. Three planes of $x = 0.7$ mm, 1.4 mm, and 2.5 mm are chosen. The top surface ($z = 0$) is indicated by the black line. From the concentration profile shown in Figs. 1 and 2, the geometry of cladding bead, including cladding depth, cladding width and cladding height can be obtained.

In laser cladding, species transportation in the molten pool can be in the form of convection and diffusion. In past work, the dimensionless Peclet number, *Pe*, was used to determine the relative importance of convection and conduction in the heat transfer in laser processing [37]. Similarly, the Peclet number for mass transfer, Pe_m, can be used to indicate the relative importance of convection flow and solute diffusion in the overall transport of solute in the molten pool [38].

$$Pe_m = \frac{uL_R}{D} \tag{18}$$

where u is the typical liquid velocity, L_R is the characteristic length taken as the pool radius, D is the mass diffusivity. The three parameters take the value of 1 m/s, 0.8 mm, 3.0×10^{-8} m^2/s, respectively. The corresponding value of Pe_m is calculated to be 2.7×10^4. Convection flow is the primary mechanism in solute distribution in the molten pool, causing efficient mixing of the base metal with the powder metal. Therefore, it is necessary to consider the convective mass transport in order to simulate the solute concentration distribution accurately. It can be observed from Fig. 1 that at the time of 200 ms, a small dilution is formed. As convection in the molten pool gets stronger, the cladding depth and cladding height increase until the molten pool is fully developed.

As a supplement, the concentration variation of carbon along the coordinate axes at different times is calculated. Fig. 3 shows the concentration variation of carbon along the y direction, the intersection of top surface and the plane with the x coordinate of 0.7 mm, 1.4 mm, 2.5 mm, respectively. For some locations, the concentration curves coincide for different times due to the lack of convection flow during solidification stage, as shown in Fig. 4(a) and (b). From the Peclet number for mass transfer, the final concentration distribution is primarily determined by the melting stage. Fig. 5 shows the concentration variation of carbon along the z direction,

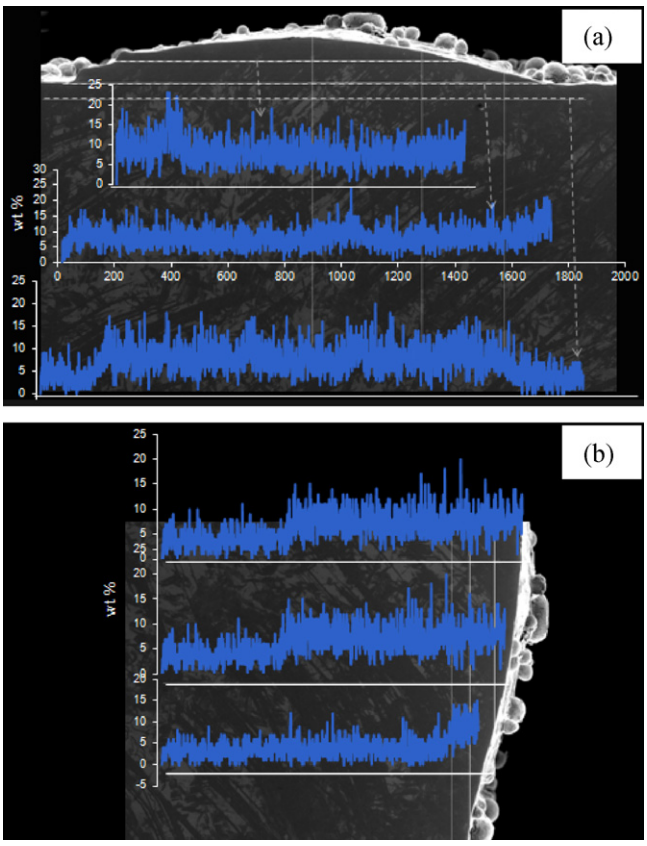

Fig. 8. Concentration of chromium (a) along the x direction and (b) along the z direction.

the intersection of symmetric plane and the same three planes. The small figure in Fig. 5(a) shows the schematic for gas phase, cladding bead and substrate. For gas phase, the carbon concentration is 0.

3.2. Concentration profile of chromium

Figs. 6 and 7 show the computed concentration profile of chromium during laser cladding at different times. The results show that the concentration distribution patterns of chromium are similar to the carbon concentration profile. This similarity is anticipated due to similar solute transport mechanism of carbon and chromium.

It should be noted that the concentration distribution of carbon and chromium is calculated by coupling solute transport with mass, momentum and energy transport equations. Actually, carbon mostly exists as carbides of chromium or iron. Some of the carbon may reside in retained austenite. In a sense, providing chromium concentration profile is more meaningful than carbon. As a supplement, the experimentally measured concentration of chromium along the x and z direction is also shown in Fig. 8.

From above results, a comparison between experimental and calculated geometry of fusion zone at vertical cross section is shown in Fig. 9. In the figure, the molten pool, represented by the zone, where the composition of chromium is higher than 0.5%, the composition of chromium in low carbon steel substrate. The computation time is 800 ms, when the molten pool is fully developed. A litter deviation of computed size and location of molten pool from experimental results is observed. This may be mainly caused by the simplicity in the simulation, which leads to the variance of some parameters in the real process from those used in the model. The effect of temperature on the thermo-physical properties and absorption coefficient of substrate and powder is ignored.

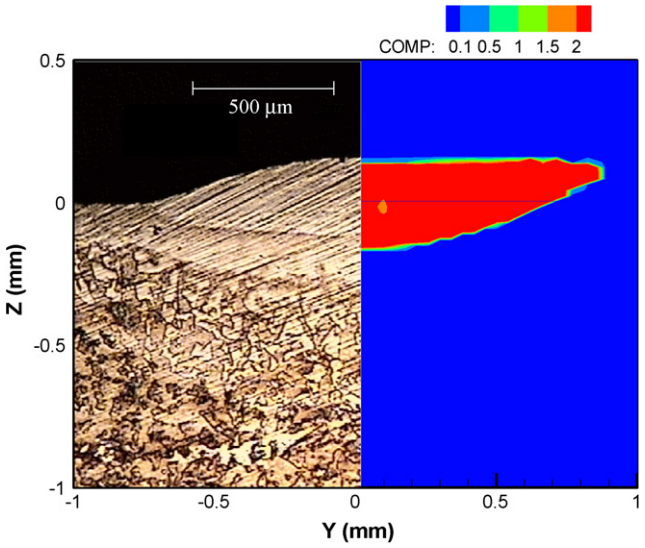

Fig. 9. Experimental and calculated geometry of molten pool.

The physical properties of the powder are assumed to be the same as those of the substrate. In addition, the spatial distribution of a converged coaxial powder flow is assumed to be Gaussian.

The composition of the alloying elements has important effects on the microstructure and mechanical performance of the deposited clad material. The numerical model is helpful in probing the underlying mechanism and the prediction of the composition profile to understand how the mechanical properties are affected by laser cladding process. The model allows calculation of acceptable range of laser cladding parameters, such as laser power and beam diameter, to attain a target composition profile. Therefore, it can be used as a tool to seek laser cladding conditions necessary to achieve an appropriate microstructure and target mechanical properties.

4. Conclusions

A self-consistent three-dimensional model has been developed to simulate the solute transport and composition profile during DMD with coaxial powder injection. The model is based on the solution of the equations of mass, momentum, energy conservation and solute transport in the molten pool, incorporating heat transfer, phase changes, mass addition, fluid flow and interactions between laser beam and coaxial powder flow. Some of the important findings are as follows:

(1) The solute transport and concentration profile of carbon and chromium during direct metal deposition are simulated. The concentration distribution pattern of chromium is similar to that of carbon due to similar solute transport mechanism.
(2) Species transportation in molten pool can be in the form of diffusion and convection in the molten pool. The Peclet number for mass transfer is in the order of 10^4, and the strong convective motion dominates the species transportation. As a result, the final concentration distribution is primarily determined by melting stage.
(3) In spite of a litter discrepancy of computed and experimental molten pool geometry due to the assumption of constant thermo-physical properties and absorption coefficient and Gaussian distribution of powder flow, the model is helpful in the prediction of the composition profile to understand how the mechanical properties are affected by DMD process.

Acknowledgements

The work is supported by a grant from the Department of Commerce Advanced Technology Program (ATP), under grant number 70NANB4H3027. Dr. Jean Louis Steademann is the Program Manager.

References

[1] X. He, J. Mazumder, Transport phenomena during direct metal deposition, J. Appl. Phys. 101 (2007) 053113.
[2] H. Qi, J. Mazumder, H. Ki, Numerical simulation of heat transfer and fluid flow in coaxial laser cladding process for direct metal deposition, J. Appl. Phys. 100 (2006) 024903.
[3] Y.L. Huang, J. Liu, N.H. Ma, J.G. Li, Three-dimensional analytical model on laser–powder interaction during laser cladding, J. Laser Appl. 18 (2006) 42–46.
[4] J.C. Liu, L.J. Li, Y.Z. Zhang, X.Z. Xie, Attenuation of laser power of a focused Gaussian beam during interaction between a laser and powder in coaxial laser cladding, J. Phys. D: Appl. Phys. 38 (2005) 1546–1550.
[5] H. Gedda, J. Powell, G. Wahlstrom, W.B. Li, H. Engstrom, C. Magnusson, Energy redistribution during CO_2 laser cladding, J. Laser Appl. 14 (2002) 78–82.
[6] J.M. Lin, Temperature analysis of the powder streams in coaxial laser cladding, Opt. Laser Technol. 31 (1999) 565–570.
[7] J.M. Lin, Laser attenuation of the focused powder streams in coaxial laser cladding, J. Laser Appl. 12 (2000) 28–33.
[8] O.O.D. Neto, R. Vilar, Physical–computational model to describe the interaction between a laser beam and a powder jet in laser surface processing, J. Laser Appl. 14 (2002) 46–51.
[9] C.Y. Liu, J.N. Lin, Thermal processes of a powder particle in coaxial laser cladding, Opt. Laser Technol. 35 (2003) 81–86.
[10] A.F.H. Kaplan, G. Groboth, Process analysis of laser beam cladding, J. Manuf. Sci. Eng.: Trans. ASME 123 (2001) 609–614.
[11] Y.C. Fu, A. Loredo, B. Martin, A.B. Vannes, A theoretical model for laser and powder particles interaction during laser cladding, J. Mater. Process. Technol. 128 (2002) 106–112.
[12] K. Partes, Analytical model of the catchment efficiency in high speed laser cladding, Surf. Coat. Technol. 204 (2009) 366–371.
[13] F. Brückner, D. Lepski, E. Beyer, Modeling the influence of process parameters and additional heat sources on residual stresses in laser cladding, J. Therm. Spray Technol. 16 (2007) 355–373.
[14] Y.L. Huang, J.G. Li, G.Y. Liang, J.Y. Su, Effect of powder feeding rate on interaction between laser beam and powder stream in laser cladding process, Rare Metal Mater. Eng. 34 (2005) 1520–1523.
[15] Y.L. Huang, G.Y. Liang, J.Y. Su, J.G. Li, Interaction between laser beam and powder stream in the process of laser cladding with powder feeding, Model. Simul. Mater. Sci. Eng. 13 (2005) 47–56.
[16] A.J. Pinkerton, L. Li, Modelling powder concentration distribution from a coaxial deposition nozzle for laser-based rapid tooling, J. Manuf. Sci. Eng.: Trans. ASME 126 (2004) 33–41.
[17] J.M. Lin, Numerical simulation of the focused powder streams in coaxial laser cladding, J. Mater. Process. Technol. 105 (2000) 17–23.
[18] J.C. Liu, L.J. Li, Effects of powder concentration distribution on fabrication of thin-wall parts in coaxial laser cladding, Opt. Laser Technol. 37 (2005) 287–292.
[19] G. Phanikumar, P. Dutta, K. Chattopadhyay, Computational modeling of laser welding of Cu–Ni dissimilar couple, Metall. Mater. Trans. B 35 (2004) 339–350.
[20] G. Phanikumar, K. Chattopadhyay, P. Dutta, Modelling of transport phenomena in laser welding of dissimilar metals, Int. J. Numer. Methods Heat Fluid Flow 11 (2001) 156–171.
[21] S. Sarkar, P.M. Raj, S. Chakraborty, P. Dutta, Three-dimensional computational modeling of momentum, heat, and mass transfer in a laser surface alloying process, Numer. Heat Tranf. A: Appl. 42 (2002) 307–326.
[22] P.M. Raj, S. Sarkar, S. Chakraborty, G. Phanikumar, P. Dutta, K. Chattopadhyay, Modelling of transport phenomena in laser surface alloying with distributed species mass source, Int. J. Heat Fluid Flow 23 (2002) 298–307.
[23] N. Chakraborty, D. Chatterjee, S. Chakraborty, Modeling of turbulent transport in laser surface alloying, Numer. Heat Tranf. A: Appl. 46 (2004) 1009–1032.
[24] S. Sarkar, P.M. Raj, S. Chakraborty, G. Phanikumar, K. Chattopadhyay, P. Dutta, Transport phenomena in laser surface alloying, J. Mater. Sci. 38 (2003) 155–164.
[25] M. Rohde, D. Dimitrova, Modelling of laser surface alloying and dispersing of ceramics, Laser Photonics Rev. 2 (2008) 290–298.
[26] A. Kar, J. Mazumder, One-dimensional diffusion model for extended solid solution in laser cladding, J. Appl. Phys. 62 (1987) 2645–2655.
[27] Y.L. Huang, Y.Q. Yang, G.Q. Wei, W.Q. Shi, Y.B. Li, Boundary coupled dual-equation numerical simulation on mass transfer in the process of laser cladding, Chin. Opt. Lett. 6 (2008) 356–360.
[28] X. He, G. Yu, J. Mazumder, Temperature and composition profile during double-track laser cladding of H13 tool steel, J. Phys. D: Appl. Phys. 43 (2010) 015502.
[29] V.R. Voller, C.R. Swaminathan, General source-based method for solidification phase-change, Numer. Heat Tranf. B: Fundam. 19 (1991) 175–189.
[30] W.D. Bennon, F.P. Incropera, A continnum model for momentum, heat and species transport in binary solid liquid-phase change systems—I. Model formulation, Int. J. Heat Mass Transf. 30 (1987) 2160–2170.

[31] W.D. Bennon, F.P.1 Incropera, A continuum model for momentum, heat and species transport in binary solid liquid-phase change systems—II. Application to solidification in a rectangular cavity, Int. J. Heat Mass Transf. 30 (1987) 2171–2187.
[32] S. Asai, I. Muchi, Theoretical-analysis and model experiments on formation mechanism of channel-type segregation, Trans. Iron Steel Inst. Jpn. 18 (1978) 90–98.
[33] M.A. Bramson, Infrared Radiation: A Handbook for Applications, Plenum, New York, 1968.
[34] A. Kar, J. Mazumder, Model for nonequilibrium partitioning during rapid solidification of binary concentrated-solutions, Acta Metall. Mater. 40 (1992) 1873–1881.
[35] S. Vanka, Block-implicit multigrid solution of navier-stokes equations in primitive varibles, J. Comput. Phys. 65 (1986) 138–158.
[36] H. Ki, P.S. Mohanty, J. Mazumder, Modeling of laser keyhole welding: Part I. Mathematical modeling, numerical methodology, role of recoil pressure, multiple reflections, and free surface evolution, Metall. Mater. Trans. A 33 (2002) 1817–1830.
[37] X. He, J.W. Elmer, T. Debroy, Heat transfer and fluid flow in laser microwelding, J. Appl. Phys. 97 (2005) 084909.
[38] S. Mishra, S. Chakraborty, T. DebRoy, Probing liquation cracking and solidification through modeling of momentum, heat, and solute transport during welding of aluminum alloys, J. Appl. Phys. 97 (2005) 094912.